Giant tunneling magnetoresistance in van der Waals magnetic tunnel junctions formed by interlayer antiferromagnetic bilayer $CoBr_2$

Y. Zhu,[1,2] X. Y. Guo,[1] L. N. Jiang,[2,3] Z. R. Yan,[2,3] Y. Yan,[1,*] and X. F. Han[2,3,4,†]
[1]*Key Laboratory of Physics and Technology for Advanced Batteries (Ministry of Education), Department of Physics, Jilin University, Changchun 130012, China*
[2]*Center of Materials Science and Optoelectronics Engineering, University of Chinese Academy of Sciences, Beijing 100049, China*
[3]*Beijing National Laboratory for Condensed Matter Physics, Institute of Physics, University of Chinese Academy of Sciences, Chinese Academy of Sciences, Beijing 100190, China*
[4]*Songshan Lake Materials Laboratory, Dongguan, Guangdong 523808, China*

(Received 29 January 2021; revised 9 April 2021; accepted 13 April 2021; published 27 April 2021)

The discovery of two-dimensional (2D) van der Waals (vdW) intrinsic magnets has opened a promising avenue to design high-performance magnetic tunnel junctions (MTJs) based on 2D materials. In this work, using first-principles calculations, it is demonstrated that bilayer $CoBr_2$ is intrinsically a magnetic semiconductor with intralayer ferromagnetic (FM) and interlayer antiferromagnetic (AFM) couplings and the interlayer AFM coupling in bilayer $CoBr_2$ is independent on the stacking orders. Moreover, using the nonequilibrium Green's function combined with density functional theory, it is found that due to the large difference between interlayer AFM and FM states of the $CoBr_2$ barrier, the conductance of spin filter (SF) vdW MTJs based on the graphene/bilayer $CoBr_2$/graphene heterostructure for the interlayer FM state of the $CoBr_2$ barrier is about 25 times that for the interlayer AFM state of the $CoBr_2$ barrier. Consequently, a high tunneling magnetoresistance (TMR) ratio of 2420% is achieved in this SF-vdW MTJ at zero bias. In particular, because the current for the interlayer FM state of the $CoBr_2$ barrier rapidly increases with the increase of bias voltage, a giant TMR ratio of up to about 38 000% can be achieved in this SF-vdW MTJ at 0.2-V bias. Our results suggest that SF-vdW MTJs formed by the interlayer AFM barrier with variable conductivity hold great potential for developing vdW MTJs with a high TMR ratio.

DOI: 10.1103/PhysRevB.103.134437

I. INTRODUCTION

Magnetic tunnel junctions (MTJs) have been implemented in magnetic read heads and nonvolatile magnetic random-access memories [1–4]. As is known, the tunneling magnetoresistance (TMR) ratio is one of the most important performance indexes of MTJs [5–7]. In the past two decades, great efforts have been devoted to achieving a high TMR ratio in MTJs both theoretically and experimentally. The conventional MTJs are formed by sandwiching a nonmagnetic insulating barrier layer between two ferromagnetic (FM) electrodes, and the TMR is the change in resistance of MTJs when the magnetization of two electrodes is aligned parallel or antiparallel. The discovery of two-dimensional (2D) van der Waals (vdW) intrinsic magnets, such as CrI_3 [8], $CrGeTe_3$ [9], Fe_3GeTe_2 [10,11], VSe_2 [12], and $MnPS_3$ [13], has opened a new avenue to explore high-performance MTJs based on 2D materials [14–35]. In recent years, 2D vdW intrinsic magnets have been used to construct vdW heterostructures to develop vdW MTJs with a high TMR ratio [23–35]. In this regard, it was experimentally reported that by using an external magnetic field to change the interlayer ordering of few-layer CrI_3 from antiferromagnetic (AFM) to FM, a high TMR ratio of 95%, 300%, and 550% is achieved in spin filter (SF) vdW MTJs based on graphene/CrI_3/graphene heterostructures with bilayer, trilayer, and tetralayer CrI_3 magnetic barriers, respectively, at zero bias [32]. In particular, several experimental works demonstrated that at optimized biasing voltage, a giant TMR ratio of up to 19 000%, 10 000%, and even 1 000 000% can be achieved in SF-vdW MTJs based on graphite/CrI_3/graphite vdW heterostructures with CrI_3 barriers of different thicknesses under a magnetic field [33–35]. Correspondingly, Heath *et al.* theoretically investigated spin-dependent transport and the TMR effect in SF-vdW MTJs based on trilayer graphene/few-layer CrI_3/ trilayer graphene heterostructures using first-principles calculations within density functional theory (DFT) and Landauer's formalism and found that the interlayer coupling of the CrI_3 barrier, despite usually being perceived as weak, is key to properly describing electronic properties and spin-dependent transport in these SF-vdW MTJs [36]. Nevertheless, there is an obvious discrepancy in interlayer coupling of few-layer CrI_3 between theoretical calculations by Heath *et al.* and experimental measurements: The theoretical calculations indicate that the interlayer FM states of AA stacked few-layer CrI_3 are more stable than the interlayer AFM ones [36–39], while the experimental measurements demonstrate that the interlayer AFM state is the most stable in few-layer CrI_3 [40,41].

*yanyu@jlu.edu.cn
†xfhan@iphy.ac.cn

 ©2021 American Physical Society

Hence, the role of interlayer coupling of the vdW magnetic barrier on spin-dependent transport in SF-vdW MTJs formed by a 2D vdW magnetic barrier has not yet been fully unveiled.

Similar to few-layer CrI_3, bulk $CoBr_2$ with a CdI_2-type structure was reported to be a vdW intrinsically magnetic semiconductor with intralayer FM and interlayer AFM couplings both theoretically and experimentally [42–44]. Also, monolayer $CoBr_2$ was theoretically predicted to be an intrinsically FM semiconductor [45,46]. These results indicate that a high TMR ratio may be achieved in SF-vdW MTJs formed by a few-layer $CoBr_2$ barrier at a biasing voltage. Meanwhile, the investigation of SF-vdW MTJs formed by a few-layer $CoBr_2$ barrier will help to elucidate the role of interlayer coupling of a vdW magnetic barrier on spin-dependent transport in SF-vdW MTJs formed by a 2D vdW magnetic barrier.

In this work, by using first-principles calculations, we demonstrate that bilayer $CoBr_2$ is an intrinsically magnetic semiconductor with intralayer FM and interlayer AFM couplings, and the interlayer AFM coupling in bilayer $CoBr_2$ is independent of the stacking orders. Moreover, using the nonequilibrium Green's function combined with DFT, a high TMR ratio of 2420% can be achieved in SF-vdW MTJs based on graphene/bilayer $CoBr_2$/graphene heterostructures at zero bias due to the large difference in electronic properties between interlayer AFM and FM states of the $CoBr_2$ barrier. More interestingly, a giant TMR ratio of up to about 38 000% can be achieved in this SF-vdW MTJ at 0.2-V bias since the current for the interlayer FM state of the $CoBr_2$ barrier rapidly increases with the increase of bias voltage.

II. COMPUTATIONAL METHOD

First-principles calculations for the structure optimization, electronic structure, and magnetism are performed with the projector augmented-wave pseudopotentials [47] and the generalized gradient approximation (GGA) with the Perdew-Burke-Ernzerhof version [48] using the Vienna Ab initio Simulation Package (VASP) code [49,50]. The interlayer vdW interactions are treated with the optB86b-vdW functional [51], and the correlation effects for the d electrons of Co are introduced by means of the GGA+U approach with the on-site effective interaction parameter $U = 3.0$ eV, which is in the range of values used in Refs. [42,45]. A plane-wave energy cutoff of 600 eV and a $13 \times 13 \times 1$ Monkhorst-Pack k point grid are used for first-principles calculations. The structure is optimized using the conjugate gradient method, and the convergence criteria for energy and force are set to be 1×10^{-6} eV and 0.01 eV/Å, respectively. A vacuum space of 15 Å is used to eliminate the spurious interaction between periodic replicas.

The spin-dependent transport calculations are performed using the NANODCAL package through the nonequilibrium Green's function combined with the DFT considering the on-site Coulomb interaction U [52,53]. The spin-resolved conductance G_σ at zero bias is calculated using the Landauer-Büttiker formula:

$$G_\sigma = \frac{e^2}{h} \sum_{k_\parallel} T_\sigma(k_\parallel, E_F), \tag{1}$$

where $T_\sigma(k_\parallel, E_F)$ is the transmission coefficient with spin σ ($\sigma = \uparrow, \downarrow$) at the Fermi level E_F and the transverse Bloch wave vector $k_\parallel$ ($k_\parallel = k_x, k_y$) and e and h are the electron charge and the Planck constant, respectively. The TMR ratio at zero bias is defined as

$$\mathrm{TMR} = \frac{(G_{\mathrm{FM}} - G_{\mathrm{AFM}})}{G_{\mathrm{AFM}}} \times 100\%, \tag{2}$$

where G_{FM} (G_{AFM}) is the total conductance of SF-vdW MTJ when the bilayer $CoBr_2$ barrier is an interlayer FM (AFM) state, i.e., the summation of spin-up and spin-down conductances for the interlayer FM (AFM) state of the $CoBr_2$ barrier.

At bias voltage V, the spin-resolved current is calculated as follows:

$$I_\sigma = \frac{e}{h} \int T_\sigma(E, V)[f_{(E-\mu_L)} - f_{(E-\mu_R)}]dE, \tag{3}$$

where $T_\sigma(E, V)$ is the transmission coefficient at energy E with spin σ under the applied bias voltage V, $f_{(E-\mu_L)}$ ($f_{(E-\mu_R)}$) is the Fermi distribution function of electrons in the left (right) electrode, and μ_L (μ_R) is the electrochemical potential of the left (right) electrode. The TMR ratio at bias voltage is defined as $(I_{\mathrm{FM}} - I_{\mathrm{AFM}})/I_{\mathrm{AFM}} \times 100\%$, where I_{FM} (I_{AFM}) is the total current for the interlayer FM (AFM) state of the $CoBr_2$ barrier, i.e., the summation of spin-up and spin-down currents for the interlayer FM (AFM) state of the $CoBr_2$ barrier.

In spin-dependent transport calculations, the cutoff energy is set to be 160 Ry, and the basis type is double-zeta polarization. A $9 \times 9 \times 1$ k mesh is used for self-consistent calculations, and the k points for the spin-resolved transmission coefficient and current calculations are $150 \times 150 \times 1$.

III. RESULTS AND DISCUSSION

Bulk $CoBr_2$ crystallizes in a CdI_2-type layered structure, which is formed by the AA stacking of weakly vdW interacting 2D $CoBr_2$ layers [42,43]. In each $CoBr_2$ layer, one Co atom layer is sandwiched by two Br atom layers through the Co-Br bonds in antiprismatic coordination, as shown in Fig. 1(a). The optimized lattice constant and Co-Br bond length of monolayer $CoBr_2$ are in agreement with previous calculations [45,46]. Consistent with the report by Ref. [46], monolayer $CoBr_2$ is found to be an intrinsically FM semiconductor, and the magnetic moment is mainly provided by the d orbits of Co atoms. In view of variations of the interlayer magnetic couplings in bilayer $CoBr_2$ with the interlayer stacking order, we calculate the energy of bilayer $CoBr_2$ with different interlayer stacking orders in interlayer FM and AFM states. Figure 1(d) shows the change in energy of interlayer FM and AFM states for a particular stacking order, with respect to the AA stacking, rigidly shifted along the high-symmetry [100] and [1$\bar{1}$0] directions. It can be seen from Fig. 1(d) that whether interlayer magnetic couplings are FM or AFM, AA stacking is the preferred stacking order of bilayer $CoBr_2$, which is in accord with the stacking order of bulk $CoBr_2$ [42,44]. Different from bilayer CrI_3 [37], the interlayer AFM state of bilayer $CoBr_2$ for all stacking orders is more stable than the interlayer FM one, which means the interlayer AFM coupling in bilayer $CoBr_2$ is independent of the stacking orders. The optimized lattice constant and Co-Br bond length of AA-stacked bilayer

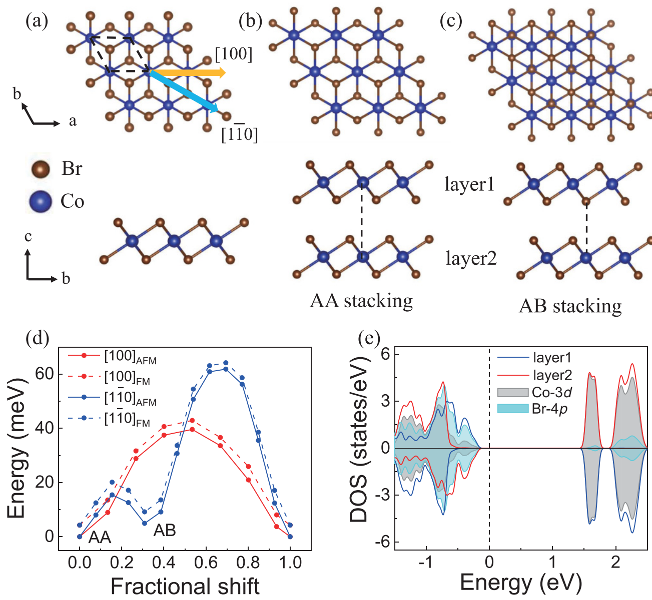

FIG. 1. Top and side views of (a) monolayer $CoBr_2$ and bilayer $CoBr_2$ with (b) AA and (c) AB stacking orders. Orange and cyan arrows indicate the [100] and [1$\bar{1}$0] directions. (d) Change in energy of interlayer FM and AFM states of bilayer $CoBr_2$ for a particular stacking order, with respect to the AA stacking, rigidly shifted along the [100] and [1$\bar{1}$0] directions. Red and blue lines represent [100] and [1$\bar{1}$0] shift directions, respectively. Solid and dashed lines represent the interlayer AFM and FM states of bilayer $CoBr_2$, respectively. (e) Layer-resolved and partial DOSs of bilayer $CoBr_2$ in the interlayer AFM state. Layer 1 and layer 2 represent the different monolayers of bilayer $CoBr_2$.

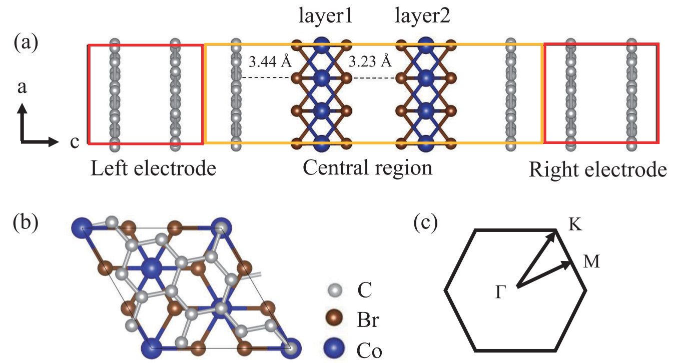

FIG. 2. (a) Side view of the atomic structure of SF-vdW MTJs based on the graphene/bilayer $CoBr_2$/graphene heterostructure and (b) top view of the graphene/bilayer $CoBr_2$/graphene heterostructure. (c) The Brillouin zone with high-symmetry points for the graphene/bilayer $CoBr_2$/graphene heterostructure.

$CoBr_2$ in interlayer AFM states are 3.74 and 2.59 Å, respectively. The same as for bulk $CoBr_2$, the interlayer distances of AA-stacked bilayer $CoBr_2$ in interlayer AFM states, i.e., the distance between the bottom Br atom layer of the upper layer and the top Br atom layer of the lower layer, is 3.24 Å. Herein, two monolayers of bilayer $CoBr_2$ are denoted layer 1 and layer 2, as shown in Fig. 1(b). The layer-resolved and partial densities of states (DOSs) in Fig. 1(e) show that bilayer $CoBr_2$ is an intrinsically magnetic semiconductor with intralayer FM and interlayer AFM couplings and the states at the conduction band minimum (CBM) are mainly contributed by *d* orbits of Co atoms.

Figures 2(a) and 2(b) show the structure of SF-vdW MTJs based on the graphene/bilayer $CoBr_2$/graphene vdW heterostructure, in which a bilayer $CoBr_2$ barrier is sandwiched between two graphite electrodes. In the vdW heterostructure, a $\sqrt{3}\times\sqrt{3}$ unit cell of $CoBr_2$ is matched at the interface with a $\sqrt{7}\times\sqrt{7}$ unit cell of graphene due to different lattice constants of bilayer $CoBr_2$ and graphene. The in-plane lattice constant of the vdW heterostructure is set to the average of the in-plane lattice constants of the $\sqrt{3}\times\sqrt{3}$ unit cell of $CoBr_2$ and the $\sqrt{7}\times\sqrt{7}$ unit cell of graphene, which yield a minimum lattice mismatch of 0.23%. The optimized interlayer distance between graphene and the $CoBr_2$ layer in the graphene/bilayer $CoBr_2$/graphene vdW heterostructure is 3.44 Å, which indicates that the interface interaction between the graphene and the $CoBr_2$ barrier layer in SF-vdW MTJs is weak. Moreover, we investigate the influences of the different values of U and vdW functionals on the calculated results of bulk and bilayer $CoBr_2$ and the graphene/bilayer $CoBr_2$/graphene vdW heterostructure. The calculations show that not only are the calculated band structures of the heterostructure and the structural parameters and magnetic property of bulk $CoBr_2$ using optB86b and optPBE vdW functionals quite similar, but also the calculated band structures of the heterostructure and the structural parameters and magnetic property of bilayer $CoBr_2$ using GGA+U with $U=2.7$, 3.0, and 3.3 eV are almost the same, which indicates that the calculated results of bulk and bilayer $CoBr_2$ and the graphene/bilayer $CoBr_2$/graphene vdW heterostructure are robust.

Table I lists the calculated conductances and the TMR ratio of SF-vdW MTJs at zero bias. It can be seen from Table I that the spin-down conductance $G_{\downarrow FM}$ is about 2 orders of magnitude larger than the spin-up conductance $G_{\uparrow FM}$ when bilayer $CoBr_2$ is the interlayer FM state; thus, the total conductance G_{FM} of the interlayer FM state of the $CoBr_2$ barrier is nearly the same as $G_{\downarrow FM}$. When bilayer $CoBr_2$ is the interlayer AFM state, the conductances for all spin states are almost equal, as shown in Table I. In particular, the total conductance G_{FM} for the interlayer FM state of the $CoBr_2$ barrier is about 25 times that for the interlayer AFM state of the $CoBr_2$ barrier, resulting in a high TMR ratio of 2420% in SF-vdW MTJs based on the graphene/bilayer $CoBr_2$/graphene heterostructure at zero bias. Corresponding to the spin-resolved conductance, Figs. 3(a)–3(d) show the distribution of spin-resolved transmission coefficients of SF-vdW MTJs for the interlayer FM and AFM states of the $CoBr_2$ barrier in the 2D Brillouin zone (2DBZ) at zero bias. It is seen from Fig. 3 that in all cases, the high transmissions are located within the small region near the high-symmetry K points. Moreover, when bilayer $CoBr_2$ is the interlayer FM state, there are relatively high transmissions for spin-down electrons in the region around the high-symmetry K and Γ points of the 2DBZ which are much larger than transmissions for spin-up electrons in these regions of the 2DBZ. Figures 3(c) and 3(d) show that the distributions of spin-up and spin-down transmissions in the 2DBZ are the

TABLE I. Calculated conductance (in units of e^2/h) and TMR ratios of SF-vdW MTJs based on the graphene/bilayer $CoBr_2$/graphene vdW heterostructure. G_{FM} (G_{AFM}), $G_{\uparrow FM}$ ($G_{\uparrow AFM}$), and $G_{\downarrow FM}$ ($G_{\downarrow AFM}$) represent the total, spin-up, and spin-down conductances for the interlayer FM (AFM) state of SF-vdW MTJ, respectively.

$G_{\uparrow FM}$	$G_{\downarrow FM}$	G_{FM}	$G_{\uparrow AFM}$	$G_{\downarrow AFM}$	G_{AFM}	TMR (%)
2.9×10^{-10}	6.3×10^{-8}	6.3×10^{-8}	1.3×10^{-9}	1.2×10^{-9}	2.5×10^{-9}	2420

same when bilayer $CoBr_2$ is the interlayer AFM state. It is known that the electron transmission across SF-vdW MTJs is related not only to the electronic properties of the bilayer $CoBr_2$ barrier and interfacial graphene in the central region but also to the intrinsic conduction channels of the graphite electrode, and the spin and transverse wave vectors $k_\parallel$ are conserved in the transmission process. In the following, we illustrate the spin-dependent conductance of SF-vdW MTJs by analyzing the conduction channels of graphite and the DOS and electronic band of the bilayer $CoBr_2$ barrier and interfacial graphene in the central region.

Figure 3(e) shows the distribution of the conduction channels of the graphite electrode in the 2DBZ at the Fermi level. It is seen that the conduction channels of graphite are mainly located at the high-symmetry K points of the 2DBZ.

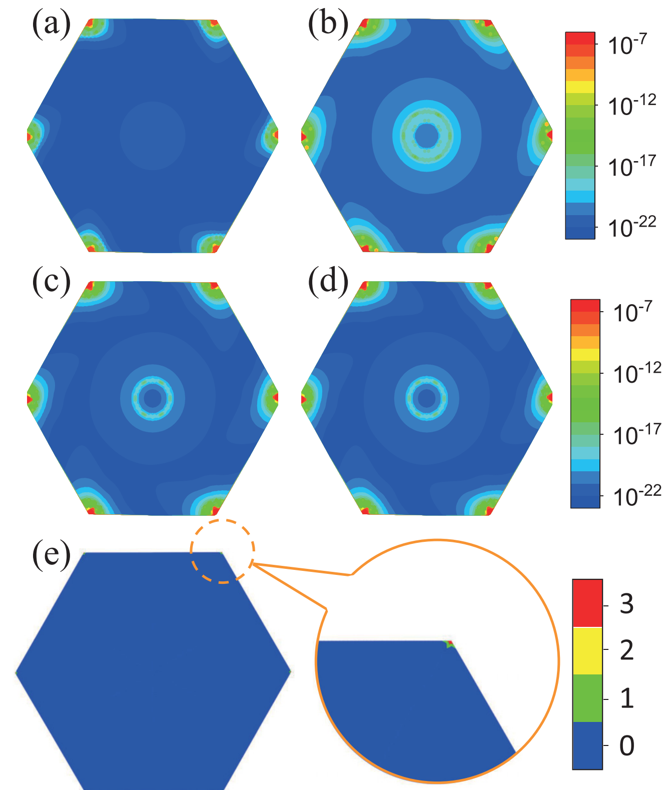

FIG. 3. The $k_\parallel$-resolved (a) spin-up and (b) spin-down transmission coefficients of SF-vdW MTJs in the 2DBZ at the Fermi level when bilayer $CoBr_2$ is interlayer FM state. The $k_\parallel$-resolved (c) spin-up and (d) spin-down transmission coefficients of SF-vdW MTJs in the 2DBZ at the Fermi level when bilayer $CoBr_2$ is interlayer AFM state. (e) $k_\parallel$-resolved conduction channels of graphite electrode in the 2DBZ at the Fermi level. The inset shows the detail of conduction channels at high-symmetry K points.

Because the conduction channels of the electrode represent the incoming and outgoing Bloch states associated with the transport across SF-vdW MTJs, the conduction channels at the high-symmetry K points result in the high transmission in the small region near the K points in all cases, as shown in Figs. 3(a)–3(d). On the other hand, the local DOS in the real space of the central region in Figs. 4(a) and 4(b) shows that when bilayer $CoBr_2$ is the interlayer FM state, the spin-down state of each monolayer of bilayer $CoBr_2$ in SF-vdW MTJs is metallic, while the spin-up state of each monolayer $CoBr_2$ is semiconducting; that is, bilayer $CoBr_2$ is a FM half metal. Meanwhile, the band structures of the central region in Fig. 5 show that the bands of interfacial graphene around the K points cross the Fermi level due to upward shift of the Dirac point. Moreover, it is seen from Figs. 5(a) and 5(b) that when bilayer $CoBr_2$ is the interlayer FM state, the spin-down bands of bilayer $CoBr_2$ around the Γ point cross the Fermi level, and the spin-down band gap of bilayer $CoBr_2$ around the K points is much smaller than the spin-up one. Consequently, the spin-down transmissions in the region around the K and Γ points are much larger than the spin-up ones in the case of the interlayer FM state of the $CoBr_2$ barrier, as shown in Figs. 3(a) and 3(b). Correspondingly, the spin-down conductance $G_{\downarrow FM}$ is much larger than $G_{\uparrow FM}$, and the total conductance G_{FM} is nearly the same as $G_{\downarrow FM}$ in the case of the interlayer FM

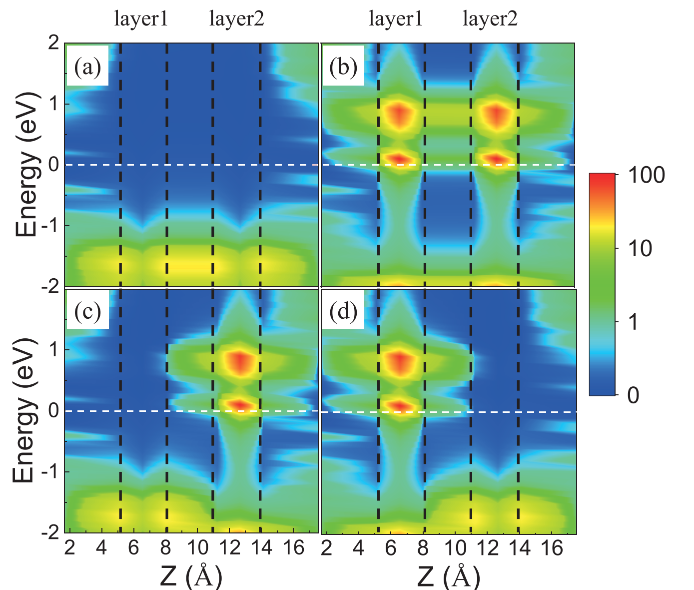

FIG. 4. Local DOS in real space along the transport direction of graphene/bilayer $CoBr_2$/graphene. (a) Spin-up and (b) spin-down DOS when bilayer $CoBr_2$ is the interlayer FM state. (c) Spin-up and (d) spin-down DOS when bilayer $CoBr_2$ is the interlayer AFM state. The Fermi level is denoted by the horizontal dashed line.

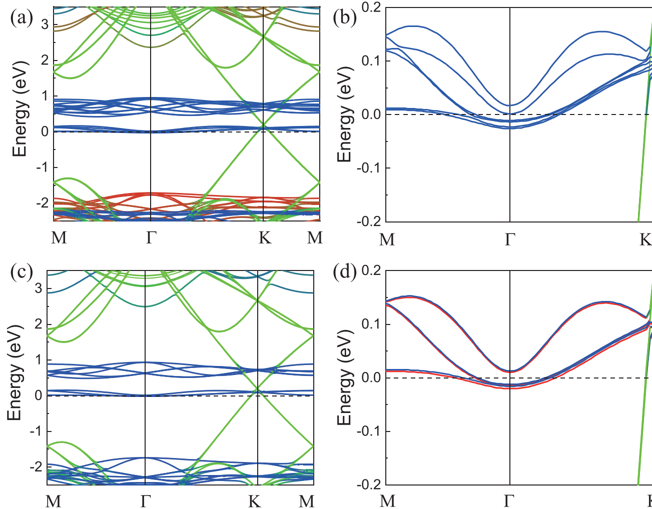

FIG. 5. Spin-resolved band structure of the graphene/bilayer $CoBr_2$/graphene heterostructure when bilayer $CoBr_2$ is interlayer (a) FM and (c) AFM states. Spin-resolved band structure around the high-symmetry Γ point when bilayer $CoBr_2$ is interlayer (b) FM and (d) AFM states. The Fermi level is denoted by the horizontal dashed line. The green, red, and blue lines represent the projected bands of interfacial graphene and spin-up and spin-down states of $CoBr_2$, respectively.

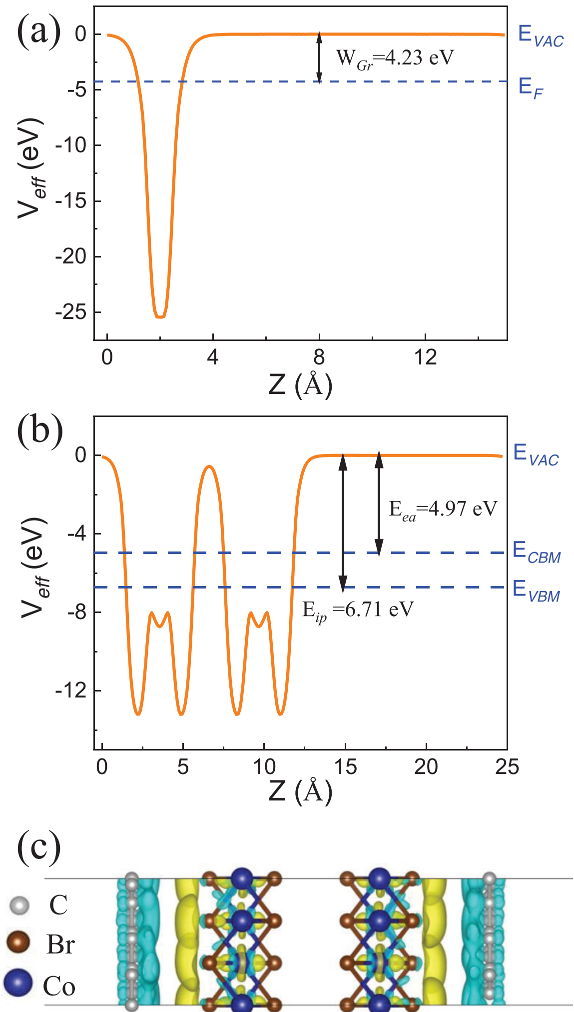

FIG. 6. Electrostatic potential V_{eff} for (a) graphene and (b) the isolated bilayer $CoBr_2$. W_{Gr} represents the work function of graphene. E_{ea} and E_{ip} represent the electron affinity and ionization potential of the isolated bilayer $CoBr_2$, respectively. E_{VAC} represents the vacuum energy level, and E_{CBM} and E_{VBM} represent CBM and VBM energies of bilayer $CoBr_2$, respectively. (c) Differential charge density of the graphene/bilayer $CoBr_2$/graphene heterostructure when bilayer $CoBr_2$ is the interlayer AFM state. The isosurface value is set to 0.0002 $e/Å^3$. Yellow and cyan represent the accumulation and depletion of electrons, respectively.

state SF-vdW MTJ. In contrast to the case of the interlayer FM state of $CoBr_2$, when bilayer $CoBr_2$ is the interlayer AFM state, if the spin-down state of layer 1 and the spin-up state of layer 2 of bilayer $CoBr_2$ are metallic, the spin-up state of layer 1 and the spin-down state of layer 2 of bilayer $CoBr_2$ are semiconducting, as shown in Figs. 4(c) and 4(d). Also, Figs. 5(c) and 5(d) show that when bilayer $CoBr_2$ is the interlayer AFM state, the spin-up (spin-down) band of layer 1 of bilayer $CoBr_2$ is almost the same as the spin-down (spin-up) band of layer 2 and branches of the spin-down band which cross the Fermi level around the Γ point are almost equal to those of the spin-up band. As a result, the transmissions for the spin channels are almost equal in the case of the interlayer AFM state of bilayer $CoBr_2$, and they are obviously smaller than the spin-down transmissions for the interlayer FM state of bilayer $CoBr_2$. Correspondingly, the conductance G_{FM} is about 25 times G_{AFM} for SF-vdW MTJs based on the graphene/bilayer $CoBr_2$/graphene vdW heterostructure.

To elucidate the reason why the $CoBr_2$ barrier in SF-vdW MTJs becomes a half metal from a semiconductor of isolated bilayer $CoBr_2$, we calculate the work function W_{Gr} of graphene, as well as the electron affinity E_{ea} and ionization potential E_{ip} of isolated bilayer $CoBr_2$. As is known, W_{Gr} is defined as the energy difference between the vacuum energy level E_{VAC} and the Fermi level E_F of graphene, and E_{ea} (E_{ip}) is the energy difference between E_{VAC} and the energy of the CBM [valence band maximum (VBM)] of bilayer $CoBr_2$. As seen from Figs. 6(a) and 6(b), W_{Gr} of graphene is 4.23 eV, while E_{ea} and E_{ip} of isolated bilayer $CoBr_2$ are 4.97 and 6.71 eV, respectively. Thus, the electrons will transfer from graphene to bilayer $CoBr_2$ in the graphene/bilayer $CoBr_2$/graphene vdW heterostructure since W_{Gr} of graphene is obviously less than E_{ea} of the isolated bilayer $CoBr_2$. Correspondingly, the calculated differential charge density in Fig. 6(c) shows that the electrons are transferred from graphene to bilayer $CoBr_2$ in the graphene/bilayer $CoBr_2$/graphene vdW heterostructure. Furthermore, the Bader charge analysis shows that about 0.076 electron is transferred from interfacial graphene to the bilayer $CoBr_2$ barrier. It is seen from Figs. 5(a) and 5(b) that the spin-down CBM is closer to the Fermi level than the spin-up one when bilayer $CoBr_2$ is the interlayer FM state; thus, the electrons are transferred from two interfacial graphene to the spin-down conduction band of bilayer $CoBr_2$, resulting in the spin-down metallic state of bilayer $CoBr_2$ and upward shift of the Dirac point of graphene away from the Fermi level. In contrast to the case of the interlayer FM state of

bilayer $CoBr_2$, when bilayer $CoBr_2$ is the interlayer AFM state, the spin-down CBM of layer 1 and the spin-up CBM of layer 2 of bilayer $CoBr_2$ are closer to the Fermi level. As a result, when bilayer $CoBr_2$ is the interlayer AFM state, the electrons are transferred from two interfacial graphene to the spin-down CBM of layer 1 and the spin-up CBM of layer 2 of bilayer $CoBr_2$, resulting in the spin-down metallicity (spin-up insulator) of layer 1 and the spin-down insulator (spin-up metallicity) of layer 2, as well as an upward shift of the Dirac point of graphene away from the Fermi level, as shown in Figs. 5(c) and 5(d). Therefore, the reason why the $CoBr_2$ barrier in SF-vdW MTJs becomes a half metal in the case of the interlayer AFM or FM state of the $CoBr_2$ barrier is the shift of electrons from interfacial graphene to the $CoBr_2$ barrier.

Experimentally, it was reported that at optimized biasing voltage, a giant TMR ratio of $10^5\%$ to $10^6\%$ can be achieved in SF-vdW MTJs based on graphene/few-layer CrI_3/graphene vdW heterostructures [33–35]. Correspondingly, the TMR ratio of SF-vdW MTJs based on graphene/bilayer $CoBr_2$/graphene heterostructures at bias voltage is calculated. Figure 7(a) shows the bias dependence of the total current for the interlayer FM and AFM states of the $CoBr_2$ barrier and the TMR ratio of SF-vdW MTJs based on graphene/bilayer $CoBr_2$/graphene heterostructures, respectively. It is seen from Fig. 7(a) that when bilayer $CoBr_2$ is interlayer FM and AFM states, the currents I_{FM} and I_{AFM} of SF-vdW MTJs almost monotonically increase with the increase of bias voltage. In particular, the current for the interlayer FM state of the $CoBr_2$ barrier rapidly increases with the increase of bias voltage when the bias voltage is larger than 0.07 V, which makes the difference between I_{FM} and I_{AFM} increase significantly when the bias voltage is larger than 0.07 V. Consequently, the TMR ratio of SF-vdW MTJs significantly increases when the bias voltage increases from 0.1 to 0.2 V, and a giant TMR ratio of up to about 38 000% is achieved in SF-vdW MTJs based on graphene/bilayer-$CoBr_2$/graphene heterostructures at 0.2-V bias, as shown in Fig. 7(a). Figure 7(b) shows the spin-down transmission coefficient of SF-vdW MTJs as a function of energy at different biases when bilayer $CoBr_2$ is the interlayer FM state, in which the transmission coefficient is the integration over all $k_{\parallel}$ points in the 2DBZ. As shown in Eq. (3), the current is obtained by integrating the transmission coefficient with respect to energies in the bias window. The energy range of the bias window is from $E_F - \mathrm{eV}/2$ to $E_F + \mathrm{eV}/2$ for a given bias voltage V. Related to transmission, Fig. 7(b) also shows the spin-down DOS of the graphene/bilayer $CoBr_2$/graphene heterostructure at different biases in the case of the interlayer FM state of the $CoBr_2$ barrier. As shown by the spin-down DOS in Fig. 7(b), as the bias voltage increases, the shift of the Fermi level significantly increases the occupied spin-down states of the bilayer $CoBr_2$ barrier, which largely enhance the half metallicity of the bilayer $CoBr_2$ barrier. Corresponding to enhancement of the half metallicity of the bilayer $CoBr_2$ barrier, the peaks in transmission are significantly increased by bias voltage when bilayer $CoBr_2$ is the interlayer FM state, as shown in Fig. 7(b). Meanwhile, it is seen from Fig. 7(b) that the positions of peaks in transmission are shifted towards the Fermi level by increasing the bias voltage and all peaks

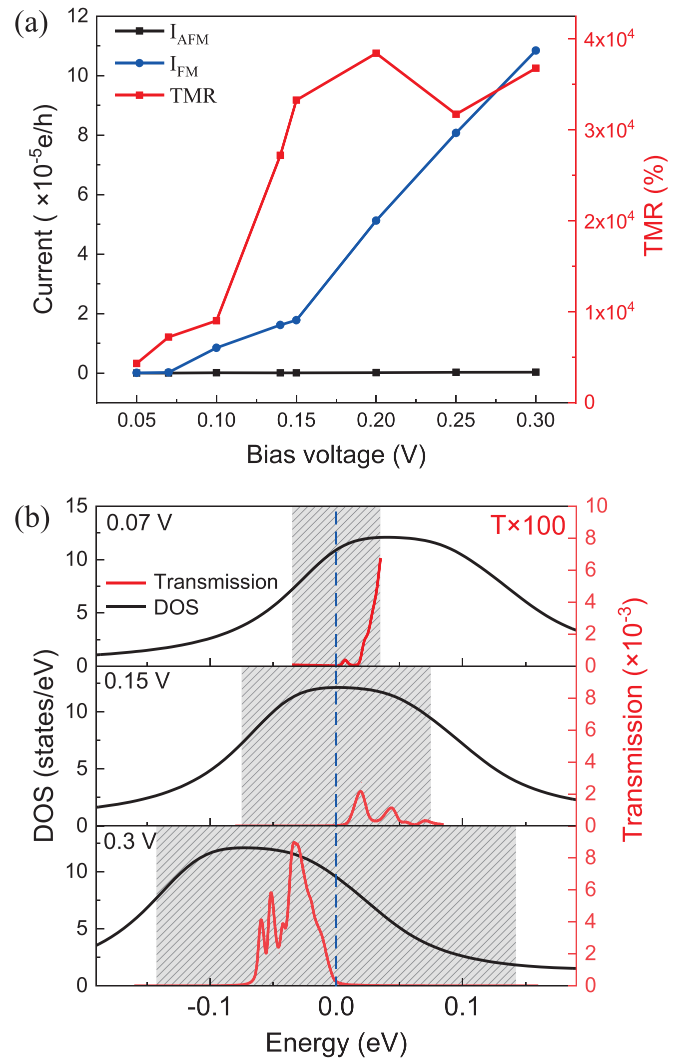

FIG. 7. (a) Total current for the interlayer FM and AFM states of the $CoBr_2$ barrier and TMR ratio of SF-vdW MTJs based on graphene/bilayer $CoBr_2$/graphene heterostructures as a function of bias voltage. (b) Spin-down transmission coefficient of SF-vdW MTJs as a function of energy at 0.07-, 0.15-, and 0.3-V bias and the corresponding spin-down DOS when bilayer $CoBr_2$ is the interlayer FM state. Transmission spectra at 0.07 V is magnified 100 times for clarity. The gray shading represents the bias window. The Fermi energy is indicated by the vertical dashed line.

in transmission are within the bias window when bias voltage increases to 0.3 V. Consequently, the integral of the transmission coefficient in the bias window increases rapidly with the increase of bias voltage, resulting in a significant increase of the current across SF-vdW MTJs at bias voltage when bilayer $CoBr_2$ is the interlayer FM state. In contrast to the significant increase of current in the case of the interlayer FM state of the $CoBr_2$ barrier, the current across SF-vdW MTJs in the case of the interlayer AFM state of the $CoBr_2$ barrier increases slowly with bias since one monolayer in the bilayer $CoBr_2$ barrier is semiconducting for one spin channel, which suppresses the current across SF-vdW MTJs in the case of the interlayer AFM state of the $CoBr_2$ barrier.

IV. CONCLUSIONS

In summary, using first-principles calculations, we theoretically demonstrated that bilayer $CoBr_2$ is an intrinsically magnetic semiconductor with intralayer ferromagnetic and interlayer antiferromagnetic couplings and the interlayer AFM coupling in bilayer $CoBr_2$ is independent of the stacking orders. Furthermore, we designed SF-vdW MTJs based on the graphene/bilayer $CoBr_2$/graphene vdW heterostructure and found that the shift of electrons from interfacial graphene to the $CoBr_2$ barrier results in the spin-down metallicity (spin-up insulator) of bilayer $CoBr_2$ in the case of the interlayer FM state of the $CoBr_2$ barrier, as well as the spin-down metallicity (spin-up insulator) of layer 1 and the spin-down insulator (spin-up metallicity) of layer 2 in the case of the interlayer AFM state of the $CoBr_2$ barrier. As a result, the conductance of SF-vdW MTJs based on the graphene/bilayer $CoBr_2$/graphene heterostructure for the interlayer FM state of the $CoBr_2$ barrier is about 25 times that for the interlayer AFM state of the $CoBr_2$ barrier, which results in a high TMR ratio of 2420% in this SF-vdW MTJ at zero bias. In contrast to the significant increase of current for the interlayer FM state of the $CoBr_2$ barrier, the current across SF-vdW MTJs in the case of the interlayer AFM state of the $CoBr_2$ barrier increases slowly with bias. Thus, a giant TMR ratio of up to about 38 000% can be achieved in this SF-vdW MTJ at 0.2-V bias. Our results provide a promising avenue for achieving a large TMR effect in vdW MTJs based on 2D vdW intrinsic magnets.

ACKNOWLEDGMENTS

This work was supported by the National Key Research and Development Program of China (MOST; Grants No. 2017YFA0206200 and No. 2018YFB0407600), the National Natural Science Foundation of China (NSFC; Grants No. 51831012, No. 51620105004, and No. 11874173), the Beijing Natural Science Foundation (Grant No. Z201100004220006), and the Strategic Priority Research Program (B) of Chinese Academy of Sciences (CAS) (Grant No. XDB33000000). The authors acknowledge the computational support provided by the High Performance Computing Center of Jilin University and National Supercomputer Center in Tianjin, and the calculations were performed on TianHe-1(A).

[1] M. Julliere, Phys. Lett. A **54**, 225 (1975).
[2] T. Miyazaki and N. Tezuka, J. Magn. Magn. Mater. **139**, L231 (1995).
[3] S. A. Wolf, D. D. Awschalom, R. A. Buhrman, J. M. Daughton, S. von Molnár, M. L. Roukes, A. Y. Chtchelkanova, and D. M. Treger, Science **294**, 1488 (2001).
[4] A. Fert, Angew. Chem., Int. Ed. **47**, 5956 (2008).
[5] W. H. Butler, X. G. Zhang, T. C. Schulthess, and J. M. MacLaren, Phys. Rev. B **63**, 054416 (2001).
[6] L. Gao, X. Jiang, S.-H. Yang, J. D. Burton, E. Y. Tsymbal, and S. S. P. Parkin, Phys. Rev. Lett. **99**, 226602 (2007).
[7] F. Bonell, T. Hauet, S. Andrieu, F. Bertran, P. Le Fèvre, L. Calmels, A. Tejeda, F. Montaigne, B. Warot-Fonrose, B. Belhadji, A. Nicolaou, and A. Taleb-Ibrahimi, Phys. Rev. Lett. **108**, 176602 (2012).
[8] B. Huang, G. Clark, E. Navarro-Moratalla, D. R. Klein, R. Cheng, K. L. Seyler, D. Zhong, E. Schmidgall, M. A. McGuire, D. H. Cobden, W. Yao, D. Xiao, P. Jarillo-Herrero, and X. Xu, Nature (London) **546**, 270 (2017).
[9] C. Gong, L. Li, Z. Li, H. Ji, A. Stern, Y. Xia, T. Cao, W. Bao, C. Wang, Y. Wang, Z. Q. Qiu, R. J. Cava, S. G. Louie, J. Xia, and X. Zhang, Nature (London) **546**, 265 (2017).
[10] Y. Deng, Y. Yu, Y. Song, J. Zhang, N. Z. Wang, Z. Sun, Y. Yi, Y. Z. Wu, S. Wu, J. Zhu, J. Wang, X. H. Chen, and Y. Zhang, Nature (London) **563**, 94 (2018).
[11] Z. Fei, B. Huang, P. Malinowski, W. Wang, T. Song, J. Sanchez, W. Yao, D. Xiao, X. Zhu, A. F. May, W. Wu, D. H. Cobden, J.-H. Chu, and X. Xu, Nat. Mater. **17**, 778 (2018).
[12] M. Bonilla, S. Kolekar, Y. Ma, H. C. Diaz, V. Kalappattil, R. Das, T. Eggers, H. R. Gutierrez, M.-H. Phan, and M. Batzill, Nat. Nanotechnol. **13**, 289 (2018).
[13] G. Long, T. Zhang, X. Cai, J. Hu, C.-w. Cho, S. Xu, J. Shen, Z. Wu, T. Han, J. Lin, J. Wang, Y. Cai, R. Lortz, Z. Mao, and N. Wang, ACS Nano **11**, 11330 (2017).
[14] G. Hu, Y. Zhu, J. Xiang, T.-Y. Yang, M. Huang, Z. Wang, Z. Wang, P. Liu, Y. Zhang, C. Feng, D. Hou, W. Zhu, M. Gu, C.-H. Hsu, F.-C. Chuang, Y. Lu, B. Xiang, and Y.-L. Chueh, ACS Nano **14**, 12037 (2020).
[15] Z. Wang, D. Sapkota, T. Taniguchi, K. Watanabe, D. Mandrus, and A. F. Morpurgo, Nano Lett. **18**, 4303 (2018).
[16] T. R. Paudel and E. Y. Tsymbal, ACS Appl. Mater. Inter. **11**, 15781 (2019).
[17] Z. Yan, R. Zhang, X. Dong, S. Qi, and X. Xu, Phys. Chem. Chem. Phys. **22**, 14773 (2020).
[18] J. Zhou, J. Qiao, C. G. Duan, A. Bournel, K. L. Wang, and W. Zhao, ACS Appl. Mater. Inter. **11**, 17647 (2019).
[19] F. Li, B. Yang, Y. Zhu, X. Han, and Y. Yan, Appl. Phys. Lett. **117**, 022412 (2020).
[20] X. Li, J. T. Lu, J. Zhang, L. You, Y. Su, and E. Y. Tsymbal, Nano Lett. **19**, 5133 (2019).
[21] L. Zhang, T. Li, J. Li, Y. Jiang, J. Yuan, and H. Li, J. Phys. Chem. C **124**, 27429 (2020).
[22] F. Li, B. Yang, Y. Zhu, X. Han, and Y. Yan, Appl. Surf. Sci. **505**, 144648 (2020).
[23] J. Yang, S. Zhang, L. Li, A. Wang, Z. Zhong, and L. Chen, Matter **1**, 1304 (2019).
[24] K. Dolui, M. D. Petrovic, K. Zollner, P. Plechac, J. Fabian, and B. K. Nikolic, Nano Lett. **20**, 2288 (2020).
[25] B. Huang, M. A. McGuire, A. F. May, D. Xiao, P. Jarillo-Herrero, and X. Xu, Nat. Mater. **19**, 1276 (2020).
[26] C. Gong and X. Zhang, Science **363**, eaav4450 (2019).
[27] X. Cai, T. Song, N. P. Wilson, G. Clark, M. He, X. Zhang, T. Taniguchi, K. Watanabe, W. Yao, D. Xiao, M. A. McGuire, D. H. Cobden, and X. Xu, Nano Lett. **19**, 3993 (2019).
[28] L. Pan, L. Huang, M. Zhong, X. W. Jiang, H. X. Deng, J. Li, J. B. Xia, and Z. Wei, Nanoscale **10**, 22196 (2018).
[29] Y. Feng, X. Wu, L. Hu, and G. Gao, J. Mater. Chem. C **8**, 14353 (2020).

[30] P. Zhao, J. Li, H. Jin, L. Yu, B. Huang, and D. Ying, Phys. Chem. Chem. Phys. **20**, 10286 (2018).
[31] E. Balci, U. O. Akkus, and S. Berber, ACS Appl. Mater. Interfaces **11**, 3609 (2019).
[32] D. R. Klein, D. MacNeill, J. L. Lado, D. Soriano, E. Navarro-Moratalla, K. Watanabe, T. Taniguchi, S. Manni, P. Canfield, J. Fernández-Rossier, and P. Jarillo-Herrero, Science **360**, 1218 (2018).
[33] T. Song, X. Cai, M. W.-Y. Tu, X. Zhang, B. Huang, N. P. Wilson, K. L. Seyler, L. Zhu, T. Taniguchi, K. Watanabe, M. A. McGuire, D. H. Cobden, D. Xiao, W. Yao, and X. Xu, Science **360**, 1214 (2018).
[34] Z. Wang, I. Gutierrez-Lezama, N. Ubrig, M. Kroner, M. Gibertini, T. Taniguchi, K. Watanabe, A. Imamoglu, E. Giannini, and A. F. Morpurgo, Nat. Commun. **9**, 2516 (2018).
[35] H. H. Kim, B. Yang, T. Patel, F. Sfigakis, C. Li, S. Tian, H. Lei, and A. W. Tsen, Nano Lett. **18**, 4885 (2018).
[36] J. J. Heath, M. Costa, M. Buongiorno-Nardelli, and M. A. Kuroda, Phys. Rev. B **101**, 195439 (2020).
[37] N. Sivadas, S. Okamoto, X. Xu, C. J. Fennie, and D. Xiao, Nano Lett. **18**, 7658 (2018).
[38] P. Jiang, C. Wang, D. Chen, Z. Zhong, Z. Yuan, Z.-Y. Lu, and W. Ji, Phys. Rev. B **99**, 144401 (2019).
[39] S. W. Jang, M. Y. Jeong, H. Yoon, S. Ryee, and M. J. Han, Phys. Rev. Mater. **3**, 031001(R) (2019).
[40] K. L. Seyler, D. Zhong, D. R. Klein, S. Gao, X. Zhang, B. Huang, E. Navarro-Moratalla, L. Yang, D. H. Cobden, M. A. McGuire, W. Yao, D. Xiao, P. Jarillo-Herrero, and X. Xu, Nat. Phys. **14**, 277 (2018).
[41] Z. Sun, Y. Yi, T. Song, G. Clark, B. Huang, Y. Shan, S. Wu, D. Huang, C. Gao, Z. Chen, M. McGuire, T. Cao, D. Xiao, W.-T. Liu, W. Yao, X. Xu, and S. Wu, Nature (London) **572**, 497 (2019).
[42] A. S. Botana and M. R. Norman, Phys. Rev. Mater. **3**, 044001 (2019).
[43] M. K. Wilkinson, J. W. Cable, E. O. Wollan, and W. C. Koehler, Phys. Rev. **113**, 497 (1959).
[44] H. Yoshizawa, K. Ubukoshi, and K. Hirakawa, J. Phys. Soc. Jpn. **48**, 42 (1980).
[45] V. V. Kulish and W. Huang, J. Mater. Chem. C **5**, 8734 (2017).
[46] H. Y. Lv, W. J. Lu, X. Luo, X. B. Zhu, and Y. P. Sun, Phys. Rev. B **99**, 134416 (2019).
[47] P. E. Blochl, Phys. Rev. B **50**, 17953 (1994).
[48] J. P. Perdew, K. Burke, and M. Ernzerhof, Phys. Rev. Lett. **77**, 3865 (1996).
[49] G. Kresse and J. Hafner, Phys. Rev. B **47**, 558 (1993).
[50] G. Kresse and J. Furthmüller, Phys. Rev. B **54**, 11169 (1996).
[51] J. Klimes, D. R. Bowler, and A. Michaelides, Phys. Rev. B **83**, 195131 (2011).
[52] J. Taylor, H. Guo, and J. Wang, Phys. Rev. B **63**, 121104(R) (2001).
[53] J. Taylor, H. Guo, and J. Wang, Phys. Rev. B **63**, 245407 (2001).